

SPIRE

**SUBJECT: Optical design.
- Diffraction analysis & design.**

PREPARED BY: Martin Caldwell

DOCUMENT No: SPIRE-RAL-DOC-000441

ISSUE: 1.0

Date: 14 June 2000

CHECKED BY:

Date:

APPROVED BY:

Date:

CONTENTS.

Summary.

1. Overview & classification of SPIRE's diffraction effects.
2. Wavefront effects.
3. Beam-shape effects.
 - 3.1 Gaussian beam quick-look.
 - 3.2 Real detector beams: smooth-wall horn, single-moded.
 - 3.3 Single-mode patterns in rest of instrument.
 - 3.4 Multi-mode patterns in FTS.
 - 3.5 Model for beam patterns on sky (PSF).
 - 3.6 Features not included.
4. Beam patterns & stray-light in telescope.
 - 4.1. Beam patterns.
5. Referenced documents.

Summary.

This report gives analyses for the effects of diffraction on the optical system performance. As such it is supplementary to the performance analysis given in the Optical Design Description.

It also estimates the diffraction-induced stray-light, which feeds in to the overall Stray-light Control document.

The particular aims of the diffraction analysis has been to characterise:

1. That the optical component aperture sizes are all sufficient that the clipping levels on the long-wavelength beam are acceptable to instrument performance.
2. The instrument spatial resolution (PSF) & aperture efficiency for the various possible detector designs, including broad-band (multi-moded) horns for the FTS.
3. What instrument nominal pupil size relative to the telescope is appropriate to optimise the throughput/stray-light trade-off.

In doing so reference is made to previous technical notes to be found in the SPIRE document database, with the important results re-printed here.

1. Overview & classification of SPIRE's diffraction effects.

The effects of concern are those arising from the diffraction-induced spreading of the point-source incident beam within the instrument. This is due to its diameter being restricted by the apertures, such that the wavelength is no longer negligibly small compared to beam diameter.

In optical systems the effect thus increases as its use is extended to longer wavelengths. For example, in the thermal infra-red region the diffraction analysis often is an 'add-on' to the standard *geometric optics* design methods of ray-tracing, and the effects are likewise considered as additional or 'stray' light. In contrast, in the mm-wave region the diffractive nature dominates the optical design, and quasi-optics rather than ray-tracing is used.

The sub-mm region used in SPIRE is something of an intermediate or crossover region, and as a result the techniques used here are a hybridisation of optical & mm-wave methods.(Ref.1).

The photometer and fourier transform spectrometer that comprise the SPIRE instrument both operate over a broad wavelength range (~ 0.2 to 0.7mm). They are both imaging systems (the FOV's are respectively 8x4 arcminutes and 2.6 arcminutes diameter), wherein the beams are relayed through several stages of imaging before reaching the detector. The optical design is described in ref.2.

As well as the 'functional' components in the optical path, i.e. powered mirrors, windows, stops, filters & the interferometer delay path, there are also several flat mirrors, used to fold the beam into the available space. Due to the constraints of the instrument size, this degree of complexity forces the instrument pupil size to be limited in terms of its diameter in number of wavelengths. At the cold stop the pupil has diameter $D \approx 20\text{mm}$, i.e. at $\lambda = 0.7\text{mm}$, $D/\lambda \sim 30$ wavelengths.

When combined with the need to keep the relative aperture of the beams to $F > 4$ (for folding and component performance), this makes the diffractive aspect significant also for the *imaging* behavior of SPIRE. The con-focal beam parameter $z_0 = 4\lambda.F^2/\pi$ is $>16\text{mm}$ for the above values, and is therefore not negligible compared to the separations of the powered mirrors (typically ~ 150 mm). As a result, the *Geometric Optics* (GO) imaging (i.e. wavefront transformation) equations have to be modified.

In SPIRE these diffraction effects are only large at the long-wavelength extreme of a broad wavelength range, and so the optical analysis methods are still the more appropriate for the overall design. Therefore the optical design of SPIRE is essentially the GO one (ref.1), plus supplementary long-wavelength analyses which are the subject of this report.

In classifying & quantifying the various effects for SPIRE it is convenient to treat the wavefront & beam shape effects separately. By *wavefront* we mean the instantaneous phase versus radial position and by 'beam shape' we mean its *amplitude* patterns, although in this report we often present this as resulting *intensity* for convenience of the user.

We consider these patterns for a worst-case which is the centre wavelength of SPIRE's longest channel, i.e. 0.5mm. Since it is a broad-band instrument the results are presented in terms relative to the same patterns for the short-wavelength (geometric optics) beam.

A third classification used here is that of effects in the FIRST telescope. This part of the analysis is done separately because (a) It is outside either instrument. (b) the larger beam size means that only 'beam-shape' effects are important (c) the effect on SPIRE is mainly stray-light.

Thus the diffraction report is divided into 3 areas:

- Wavefront effects in SPIRE.
- Amplitude (beam-shape) effects in SPIRE.

- Beam-shape effects in telescope, leading to stray-light.

2. Wavefront effects.

The sizes of these effects are summarised in table 1 at the end of this section.

The important effects are:

- FTS apodisation due to finite beam-size alone.

The ray-trace layout of the FTS is shown in fig.1.

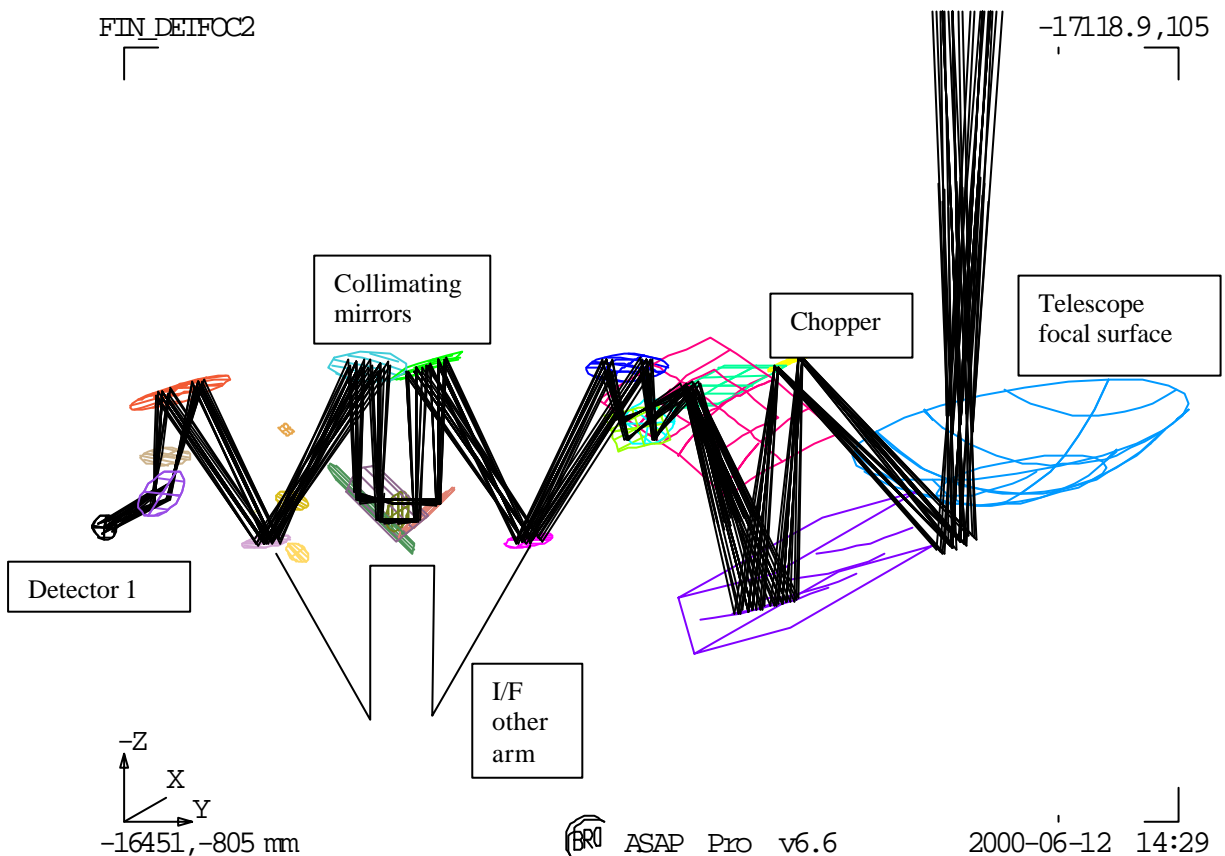


Fig.1. FTS ray-trace. File BOLSP501. Traced at + - X & + - Y edges of FOV (input beam). The interferometer section lies in the Z-Y plane.

The diffraction limitation on spectral resolution, due to the beam size, can be described in parametric terms, assuming a particular beam shape (usually gaussian). The $d=3\text{cm}$ collimated beam size ($2w$) gives a wavefront defocus of 0.016λ , and diffraction limited $R < 2 \cdot \pi A / \lambda^2 = 20,000$ at $A = \pi d^2 / 4$ and $\lambda = 0.5\text{mm}$ (refs. 2 & 3).

- FTS apodisation due to finite beam-size & FOV.

This effect can be described with geometric optics & it is dealt with in the main optical design (ref.2). That note gives a result that for $R=1000$ at $\lambda=250\mu\text{m}$ and $\text{FOV}=1.3$ arcmin radius, we require $d > 25\text{mm}$. In addition the numerical beam propagation model has been run for gaussian beams, and shows that the fringe visibility γ is reduced at max. OPD & FOV to 85% of its zero-OPD, on-axis value (ref.4).

The remaining effects in this category affect both FTS & photometer instruments, and a ray-trace of the photometer is shown in fig.2.

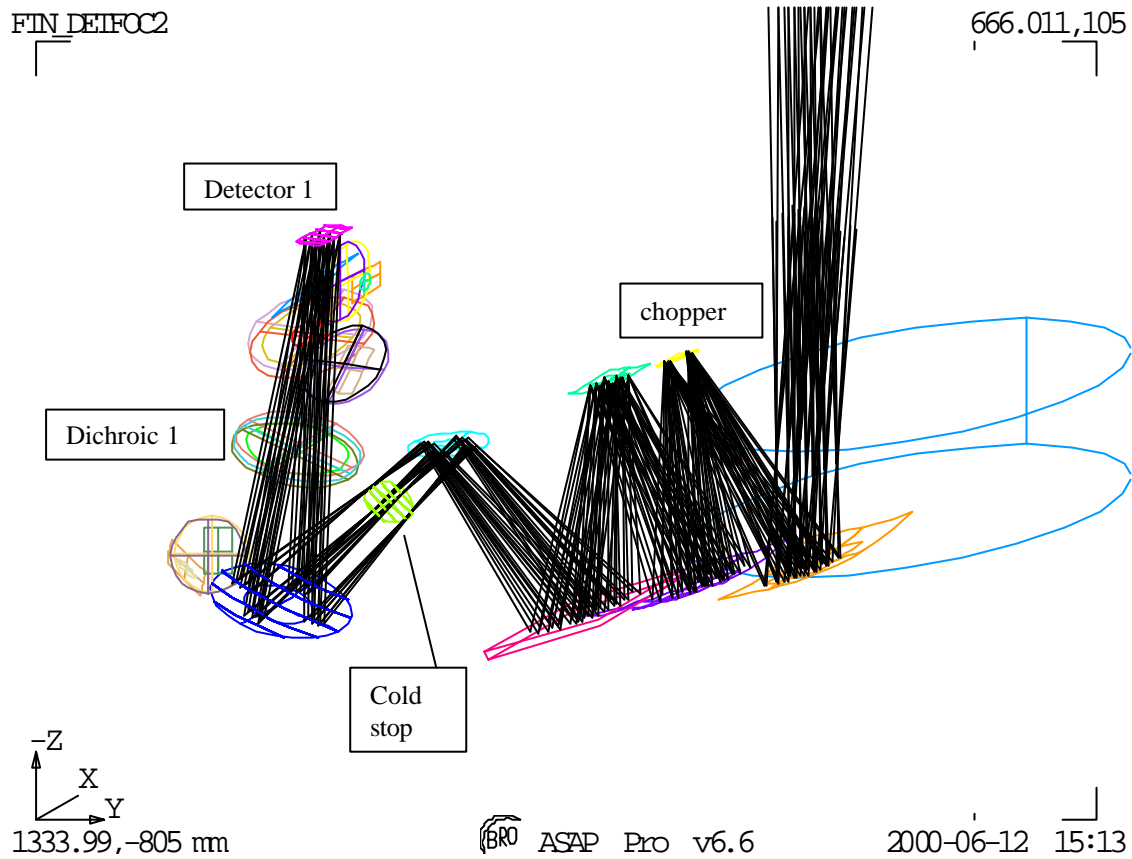


Fig.2 Photometer ray-trace. File Bolpht153. Case of 4 x 4 arcmin square FOV.

- Long-wavelength imaging.

The powered optical system images gaussian beam waists to locations which differ from the geometric optics image or pupil planes. In addition for off-axis powered reflectors this defocus can be different in the sagittal & tangential planes, leading to astigmatism in the beam. In SPIRE the image-plane deviation i.e. *defocus* is in all cases small at < 5mm (ref.3), and its astigmatism is kept small since the reflectors are anamorphic (e.g. toroid or ellipsoid) rather than spherical.

The size of this defocus is significant for correct focussing, i.e. obtaining maximum aperture efficiency, with horn detectors (ref.5), and so it is to be included in the final focus adjustment. It affects both instruments, but with different focus criteria, since in the photometer the horn is narrowband, whereas in the FTS it is broadband & in some cases also multi-mode (section 3).

- Long-wavelength aberration.

This is a knock-on effect from the above, arising as a long-wavelength coma aberration due to the wavefront ROC being no longer ideal for the conicoid mirror conjugates. In SPIRE these aberrations are very small (ref.1, tabled below).

Table 1 summarises the parameters & size of the wavefront effects.

Effect	Parameters	Size	Comment/ref
Diffraction-limited apodisation in FTS.	3cm beam $\lambda=0.5\text{mm}$ OPD=125mm Gaussian beam	$\sim 0.016\lambda$	Ref.3.
FOV- induced apodisation.	As above + FOV=1 arcmin radius Gaussian beam	Visibility $\gamma \rightarrow 85\%$	Ref.4. NOT-0269
LW defocus	$\lambda=0.5\text{mm}$ gaussian beam	-0.6mm at telescope focus -3.7mm at FTS detector	Ref.3.
LW coma aberration	$\lambda=0.5\text{mm}$ Fno = 5	$< \lambda/400$ per component	Ref.1.
	($\lambda=5\text{mm}$)	($\lambda/15$)	

Table 1. Summary of wavefront effects in SPIRE.

These estimates of wavefront effects are based on a gaussian beam shape, without truncation. I.e. they strictly apply only to a system having a perfect gaussian-mode horn detector (un-truncated) placed in a system with all apertures oversized such that their effect is negligible.

Because the effects are all quite small it is not necessary to repeat the calculations for the actual beam shape, which is discussed in the next section.

3. Beam-shape effects.

THE BEAM SHAPE (INTENSITY PATTERN) MUST BE CONTROLLED IN ORDER TO OPTIMISE

1. Stray-light.
2. Instrument PSF (spatial resolution).

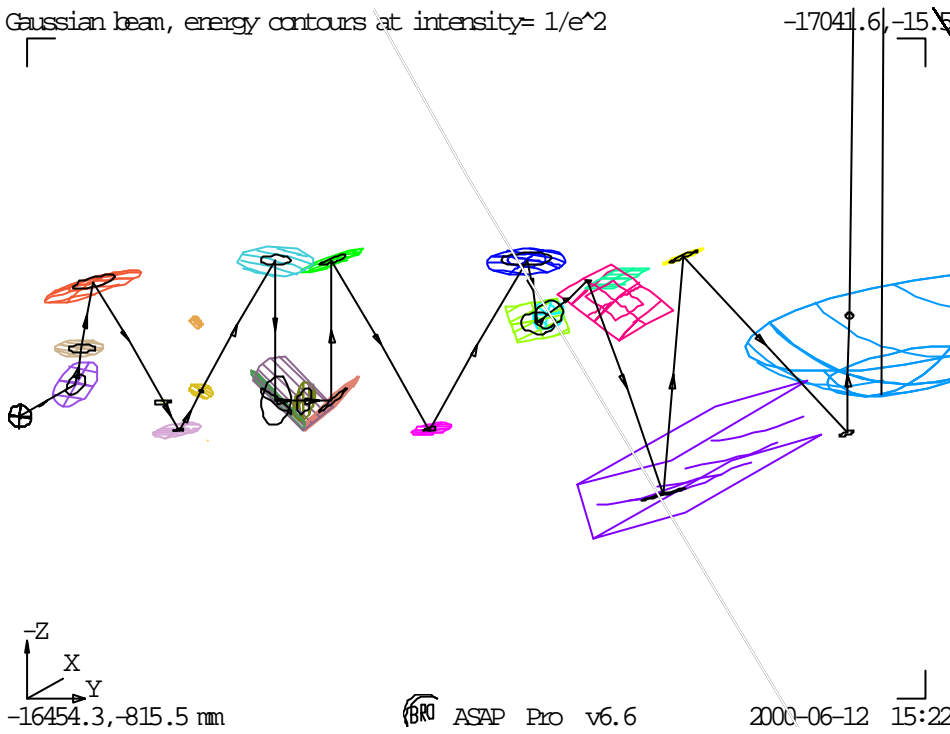
In particular the clipping of the beam pattern by apertures tends to add stray light according to the emissivity & temperature of the aperture surround, & to degrade (widen) the spatial response function (PSF) & change its shape, in the same way that aberrations do. It may also add sidelobes.

3.1 Gaussian beam quick-look plots.

In the simplest approximation (as per the last section) the beam in SPIRE is a single-mode gaussian at the horn aperture, not truncated. It is sized with waist $w_0 = (2/\pi)F\lambda$, such that in the far-field its $1/e^2$ angular diameter matches the image-space F-number of the optics ($F \approx 5$ here), so that the intensity truncation level (edge taper) at the system pupil stop is at this level. We then obtain near-optimum coherent coupling (detection efficiency) for the point-source incident beam at that F-number (an Airy pattern at the horn with 1st dark ring of diameter $1.22F\lambda$) (ref.5).

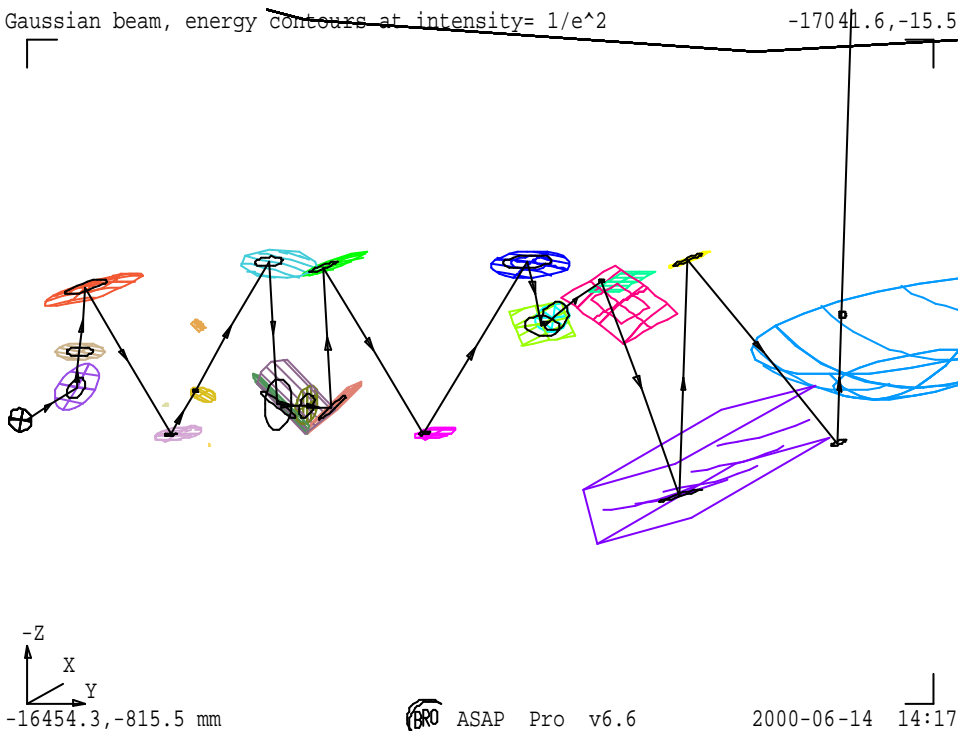
In fig.3 the $1/e^2$ intensity contour for this optimum beam is plotted throughout each instrument. This type of plot is to provide a 'quick look' for the long-wavelength beam extent, as a guide to show which are the critical components in terms of sizing, i.e. which components are in danger of clipping the beam & possibly generating stray-light or spatial response degradation.

Gaussian beam, energy contours at intensity= 1/e²



(a) spectrometer, on-axis beam

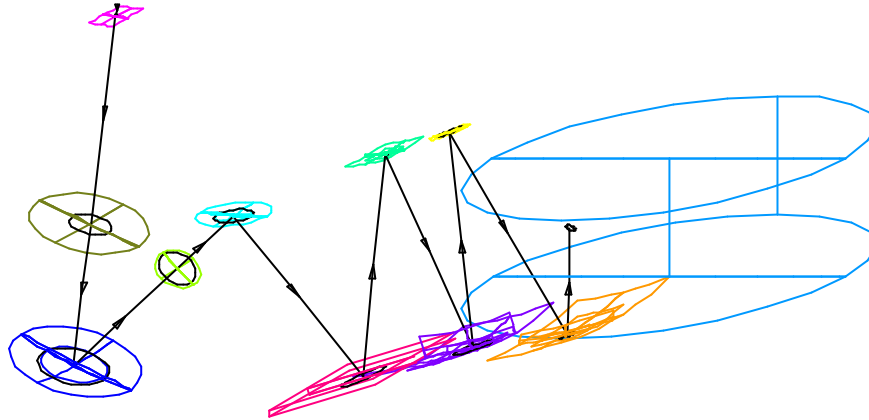
Gaussian beam, energy contours at intensity= 1/e²



(b) spectrometer, + Y detector extreme FOV

Gaussian beam, energy contours at intensity= $1/e^2$

666.011,105



1333.99, -805 mm

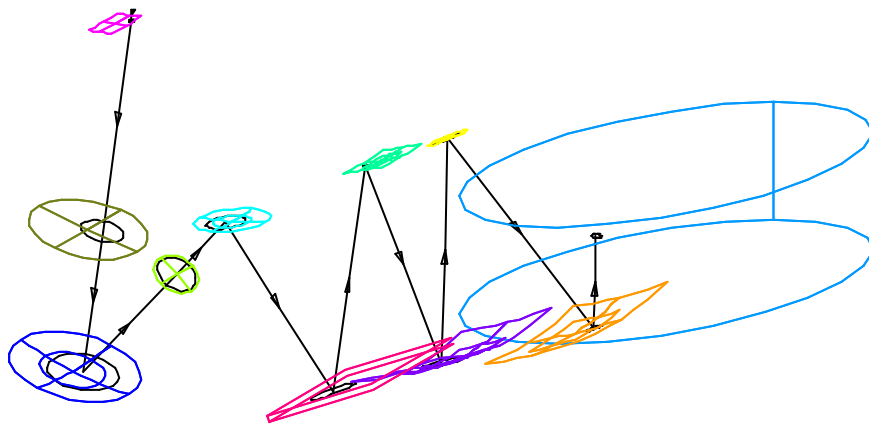
BRD ASAP Pro v6.6

2000-06-12 15:25

c) Photometer, on-axis beam.

Gaussian beam, energy contours at intensity= $1/e^2$

666.011,105



1333.99, -805 mm

BRD ASAP Pro v6.6

2000-06-14 14:04

(d) Photometer, +X, +Y corner of detector FOV position.

Fig.3. Gaussian beam quick-look plots showing $1/e^2$ intensity contour (black ellipses) at each component, $\lambda=0.5\text{mm}$. (a) FTS on-axis (b) FTS edge of FOV (c) Photometer, on-axis (d) Photometer corner of FOV.

In these plots the gaussian contour is very small at image (field stop) components, and approaches the component size at pupil stops as expected.

It can be seen that in the worst case shown, which is off-axis beam at longest wavelength, the component edges are well outside of the $1/e^2$ envelope. A basic design aim is that each component is oversized by at least 20% with respect to the geometric optics (i.e. ray-trace) beam to minimise this clipping. For the case of a component in the far field this would correspond to clipping the gaussian at 5.6 % intensity

This simplest model does not take into account the real detector beam shape, nor the added beam spread in the instrument due to the $1/e^2$ truncation of the gaussian by the cold stop.

3.2 Real detector beams: smooth-wall horn, single-moded.

For the smooth-wall circular horns in SPIRE the actual beam at the detector is shown in fig.4 for the single-mode (TE₁₁) case. The X-polarisation field is gaussian like, but with astigmatism, giving average amplitude $\sim 20\%$ around the aperture edge. This mode is propagated in reverse through the instrument, to give the detector beam pattern on each component.

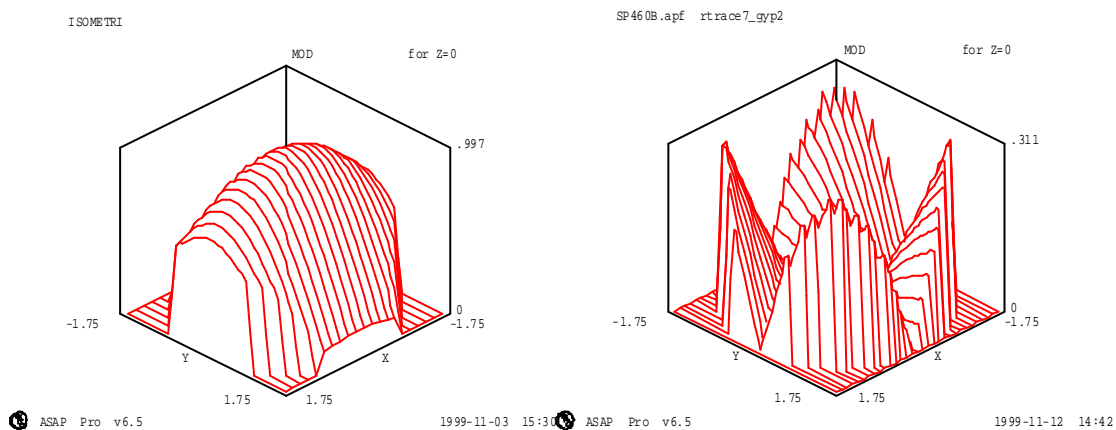
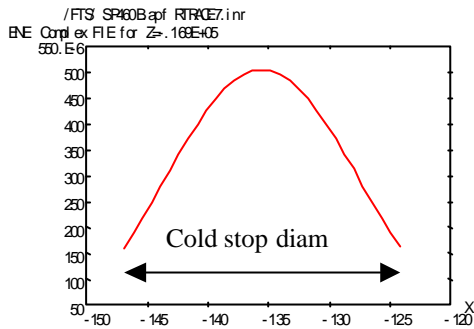


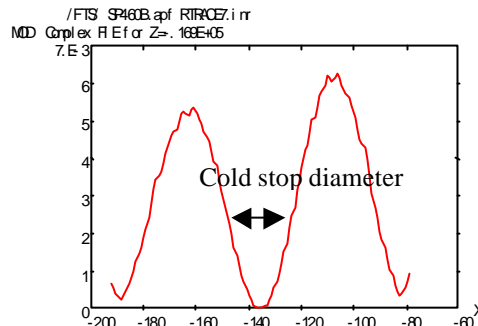
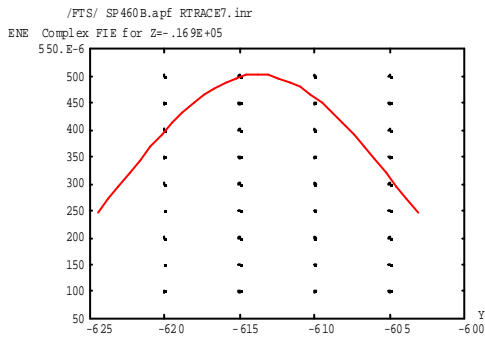
Fig.4. Beam-shape (modulus) pattern at detector, for single-mode smooth-wall horn case, TE₁₁ mode. Case is 0.35mm channel in FTS; single-moded with diameter at $2F\lambda = 3.5\text{mm}$. Plots are the cartesian polarisations E_x (at left) & E_y (at right).NB (max E_y /max E_x) $\sim 30\%$.

Note in all beam pattern plots the horizontal scale is position in millimetres.

The condition for optimum detection efficiency (pupil edge-taper $\sim 1/e^2$) is that the horn aperture size is set close to $2F\lambda$. Also that the horn length should be $L \gg$ aperture size (ref.5). In the long-wavelength case $\lambda=0.5\text{mm}$ and $L=30\text{mm}$, the actual beam pattern & clipping at the cold stop is as per the pattern of fig.5.



ASAP Pro v6.5 2000-02-03 17:13



ASAP Pro v6.5 2000-02-03 17:13

1999-11-11 17:45

(a)

(b)

Fig.5. Beam patterns at FTS Cold stop (diameter 22mm) (a) 'Ex' intensity plotted in sections versus X & Y. (b) Ey modulus plotted versus direction of maximum (diagonal to X & Y). Note: Ratio of maximum intensities is $E_x^2/E_y^2 = 500e-6/(6e-3)^2 = 14$.

The Ey has a peak intensity that is approx 1/14 th of that in Ex, and it also has a zero in the region of the ~20mm diameter cold stop. For these reasons its contribution to total field is negligible for components after to the cold stop, and so only Ex is propagated further (ref.5).

Other pupil edge-taper levels are possible, e.g. by varying the smooth-wall horn length or using corrugated horns. Their stray-light/ aperture efficiency trade-offs are being investigated, but the above is the current baseline single-mode case.

Also for the FTS broad-band horn design, there is multi-moding which further complicates the detector beam pattern.(Ref.5), and this is described in section 3.4.

3.3 Single-mode patterns in rest of instrument.

For the above long-wavelength single-mode detector beam the beam-shape plots at the other key components through the instruments are too numerous to reproduce here, but are to be found in refs. 5 & 6 for the current FTS & the photometer respectively. These are given in the sequence of the propagation analysis, i.e. outwards, up to the pick-off mirror image plane. Patterns for the telescope (case of bare detector) are presented in section 4.

In order to determine compliance with the no-clipping requirement, each pattern has to be compared with the oversize margin of that component. The asymmetry of the smooth-wall horn beam gives different beam shapes, depending on how the horn is oriented with respect to the system, and ref.6 gives the data for both orientations of the horn polarisation axes with respect to photometer symmetry plane.

The oversize margin or 'clearance' is computed from the optical ray-trace models (files as per figs 1 & 2), by calculating the beam GO footprint diameter, its distance from the component centre at edge of FOV, and the component aperture radius. The results are shown in table 2a & 2b for each instrument. For the spectrometer, the calculation is made in one radial direction only, but for the photometer with its rectangular FOV for components beyond the chopper pupil, both directions are calculated.

Component	ASAP comp't no	Field radius	Aperture diameter	GO beam diameter	Clearance margin	Clearance factor
Telescope FP	0	0				
object no	4	11.20057		11.56		
Chopper pupil	5	0.197272	30	25.3	2.152727	0.170176
	6	10.49342	204	35	74.00657	4.228947
Pick off FS	7	6.130514	52	1.42	19.15948	26.98519
	8	7.323864	95.4	3.27	38.74113	23.69488
	9	0.161589	23	15.2	3.738410	0.491896
	10	1.704701	51.25	28.5	9.670298	0.678617
	11	4.331091	66.1	38.3	9.568908	0.499681
input bs	12	6.261158	30	7.1	5.188841	1.461645
collimator	13	8.119181	51	24.2	5.280818	0.436431
	14	1.971226	41	24.2	6.428773	0.531303
	15	0.632711	32	24.2	3.267288	0.270023
pupil	0	0	0	9.5	0	0
	17	1.320089	20	24.2		
	0	0	0	9.5	0	
	19	0.987762	21.4	24.2		
	0	0	4		0	
output collimator	21	6.881083	61.2	24.25	11.59391	0.956199
output image plane	22	6.655590	20	0.22	3.234409	29.40372
output bs	23	6.657368	36	7	7.842631	2.240751
focus mirror	24	6.400455	76.2	34.3	14.54954	0.848369
Cold stop	25	1.985169	37	22.4	5.314830	0.474538
	26	0.612340	44.8	16	13.78765	1.723457
Detector	27	6.170167	23.1	0	5.379832	#DIV/0!

(a) Spectrometer

SPIRE

Project Document

Optical design, - Diffraction analysis and design

Ref: SPIRE-RAL-DOC-000???

Issue: 1.0

Date: 14th June 2000

Page: 14 of 27

Component	Component No.	X field radius	Y field radius	aperture X-radius	aperture Y-radius	GO beam X-radius	GO beam Y-radius	X-clearance	Y-clearance	Clearance X-fraction	Clearance Y-fraction
M2	0	0	1034.187	155.2	155.2						
TELESCOPE Focus	3	33.01805	19.77956	124			0.27				
	4	34.01309	17.51396	61	40.5	5	5.4	21.98690	17.58603	4.397381	3.256673
Chop PUPIL	5	0.219728	4.23E-02	15	16	11.5	11.7	3.280271	4.257688	0.285241	0.363904
	6	15.9	15.84780	40.25	42.5	17	17.5	7.35	9.152196	1.864587	0.522982
Pick-off F-S	7	9.55	10.73110	11.5	13.5	0.1	0.175	1.85	2.593897	37.98237	14.82227
	8	13.3	20.50534	59	50.5	20.5	19.8	25.2	10.19465	0.580278	0.514881
	9	2.75	4.620095	30	30	17	17.25	10.25	8.129904	0.441164	0.471298
COLD STOP	10	0.260219	0.202834	24	20.5	22	19	1.739780	1.297165	0.079080	0.068271
FOCUS MIRROR	11	5.655	7.250579	56	56	31	32.6	19.345	16.14942	0.441454	0.495380
DETECTOR	12	9.35	9.362099	11	11	0.05	0.05	1.6	1.587900	64.33815	31.75801
DICHROIC	13	7.22	8.250406	40	40	18.3	19.4712	14.48	12.27839	0.396843	0.630592

(b) Photometer.

Table 2. Beam clearance data (mm), for each component (a) spectrometer 2.6' FOV (b) photometer. FOV =rectangular X by Y = 8' by 4' up to chopper, = 4' by 4' thereafter

The final columns of each table (data in bold) show the clearance as a fraction of the GO beam radius. This fraction is to be compared with the beam pattern data (refs.5 & 6) to determine if it is sufficient.

For the spectrometer there is a question as to whether the multi-mode beam pattern (section 3.4) should be used instead, i.e. whether the multi-moding at shorter wavelengths produces wider beams than the single-mode at long wavelength. Here we assume it does not & so only the 500um single-mode patterns are tested.

In all cases (except pupil stops) the clearance fraction is > 20% i.e. better than the design goal, and this is found to be sufficient to reduce clipping of the long wavelength single-mode beam to <1 % intensity.

An example & potential worst case identified is that of the FTS beamsplitter, where because we are relatively close to an image plane (near field) the beam's wings extend well beyond its GO size, as shown in the figure 6 below.

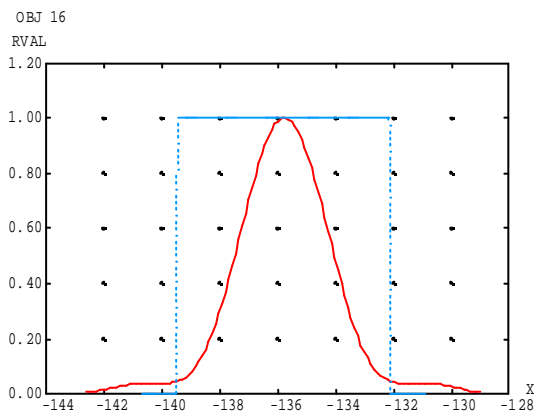
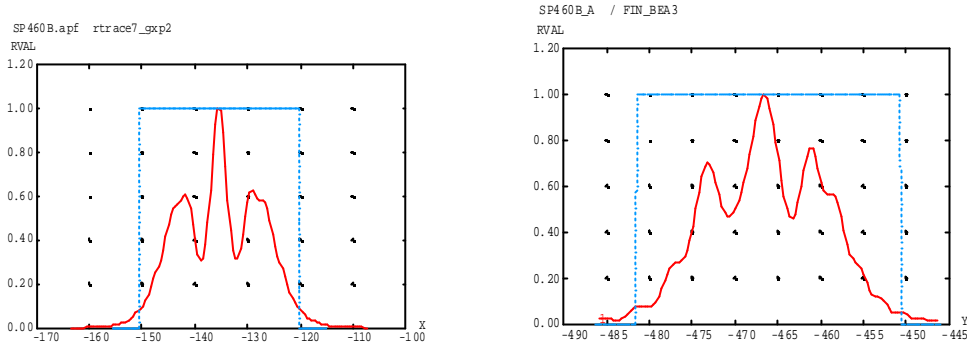


Fig.6. FTS input beamsplitter pattern, single mode, 0.5mm wavelength. GO beam shown as top-hat.

For this component table 2a gives 146 % clearance ,i.e. the component edge is at 2.46 x GO beam radius.

Also of concern is the FTS collimating mirror, whose pattern is shown below in both X & Y sections.



ASAP Pro v6.5

2000-06-13 11:33 ASAP Pro v6.5

2000-06-13 11:40

Fig.7. FTS collimator mirror.

Here the 43 % clearance (table 2a) gives clipping $\ll 1\%$. In this case however the ‘spillover’ part of the beam hitting the input collimator is not all incident on black surround, the clipped part of it lies on the adjacent mirror, i.e. the output collimator. Its reflection should be trapped by the baffle surrounding that collimator to prevent any ghost signal.

3.4 Multi-mode patterns in FTS.

The spectrometer is required to cover its broadband range (200 to 670 μm), with just 2 detector designs (2 arrays), and as a result a single detector is required to cover 350 – 670 μm . This has its entrance aperture sized at $2F\lambda$ for a design wavelength of $\lambda_{\text{des}}=0.35\text{mm}$, but its exit (& connecting waveguide) aperture is made larger than would be the case for a narrowband design, in order to pass a mode up to the longest wavelength 0.67mm. As a result the horn is multi-moded at the short wavelength end, passing 1 & 3 modes at wavelengths of >0.5 and 0.35mm respectively. (In contrast the photometer has separate detectors for each of the 3 wavelength channels, and each can be separately optimised for single-moded operation over a narrower band).

The beam patterns & aperture efficiency for such a detector have been calculated across the band, but only at spot wavelengths of 350,500 &670 μm . The mode forms & results are detailed in ref.5 & ref.1, and are summarised here.

The 3 modes involved are the lowest order (TE₁₁) & the TM₀₁ & TE₂₁ modes. Unlike the TE₁₁ mode (section 3.3) the higher order modes have polarisation that is more evenly split between the two principal directions E_x & E_y , and so both polarisations have to be propagated throughout the instrument. Because in SPIRE the source is considered to be unpolarised, it is appropriate to plot beam intensity as polarisation-averaged.

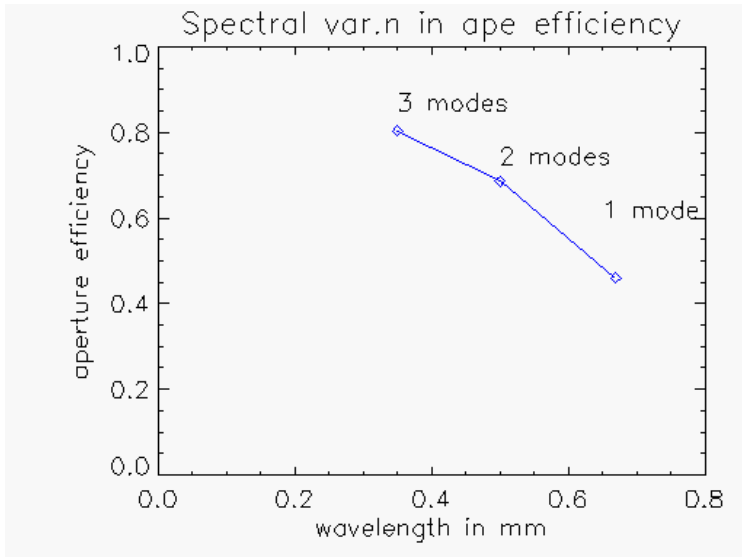
In order to calculate multi-mode beam patterns we need to know how the individual modes sum to give the net beam pattern. The multi-mode detector beam has intensity given by the sum of the individual mode intensities with equal weights, under the assumptions that the detector is an ideal bolometer (energy sensor), & that its sensitivity, and the losses in the waveguide, are independent of wavelength and mode number.

The multi-moded aperture efficiency for intensity detection is given by a sum over modes (ref.10) & for incoherent mode addition the sum is

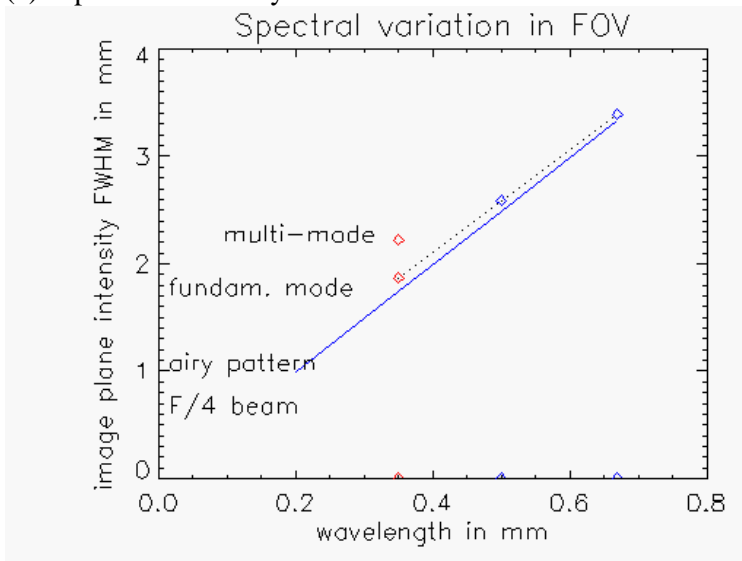
$$h = \sum_{p=0}^{\infty} |A_p \cdot C_p|^2$$

where A_p is the normalised mode amplitude and C_p is its amplitude aperture efficiency. The polarisation-averaged aperture efficiency is for the single mode case ($p=0$) $\eta = |C_0|^2 = 81\%$ at the design wavelength for a horn of infinite length, and increases by approx. 7% when the 2 higher order modes are included.

Figure 8a shows the actual efficiency plotted versus λ for a horn of length $L=30\text{mm}$, (for which the single-mode efficiency drops to 73%). The reduction in efficiency at longer wavelength is due partly to the fewer modes propagating, but is mainly due to loss of efficiency in the single-mode case, as the incident beam Airy disc at the horn becomes increasingly oversized with respect to the horn aperture.



(a) Aperture efficiency

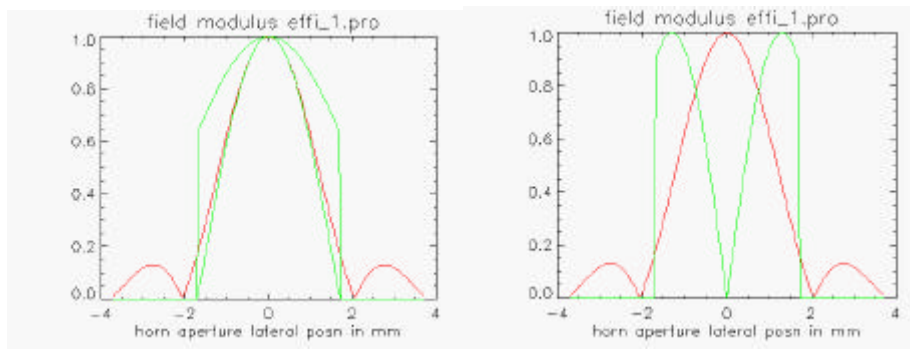


(b)

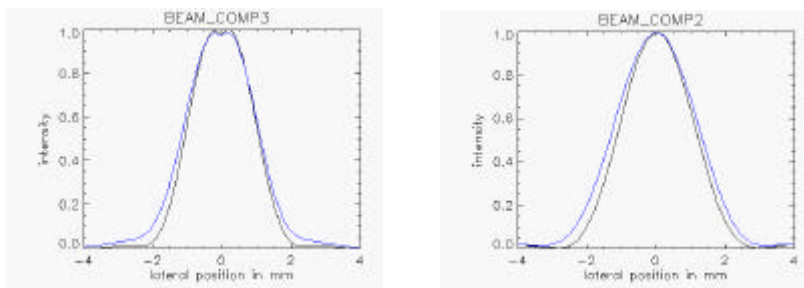
Figure 8. Spectral variations of broad-band horn design.

The multi-mode beam pattern is taken as the intensity (i.e. incoherent) sum of the modes, weighted according to mode intensity efficiencies, i.e. the $|C_p|^2$.

Figure 9 shows at $\lambda=350\mu\text{m}$ the individual mode patterns (and incident beam) at the detector, plus the resulting multi-mode beam pattern at the instrument field stop (pick-off mirror). The clipping by the cold stop is to preferentially attenuate the higher order modes (the intensity efficiency is approx. $\frac{3}{4}$ that of the TE11), and the multi-mode pattern at the field stop retains much of the gaussian-like shape of the TE11 alone. Its FWHM is approx. 20% wider, as shown in figure 8b which summarises the trend in field-stop beam FWHM versus wavelength. This parameter is important because when scaled onto the sky (see next section) it is indicative of spatial resolution (PSF width). Also plotted on figure 8b is the same parameter for an Airy pattern beam of this F-number, i.e. indicating the maximum possible spatial resolution (diffraction-limited), obtainable by fully filling the aperture (using bare detectors of size $\ll 2F\lambda$).



(a) Detector beam patterns. $\lambda=0.4\text{mm}, F=4$ Airy pattern in red. Horn mode in green, in X- & Y-sections.
 Left: single mode TE11. Right: TM01 & TE21 where pattern in x- & y-section is the same



$\lambda=0.35\text{mm}$, 3 modes

$\lambda=0.5\text{mm}$, single mode

(b) Field stop (pick-off) patterns (in X- & Y- sections) at different wavelengths.

Fig.9. Multimode beam patterns (a) individual modes at detector where for the higher order modes the pattern in x- or y-section is the same (b) multi-mode patterns at field stop. In this previous design SP460B, the magnification=1 between detector & field stop planes (beam $F=4$ in each).

Note that this analysis is for the on-axis detector beam, which has minimum aberration. The effect of increased aberrations in the off-axis case degrades the PSF (ref.2).

The summary data of fig.8 shows that to obtain a broad-band smooth-wall horn detector in this region, at the design (shorter) wavelength we lose approx. 20 % in spatial resolution (PSF FWHM), and at longer wavelength we lose efficiency, as compared to the use narrower-band (single-mode) horn design at either wavelength.

3.5 Model for beam patterns on sky (PSF).

In the current model the *cold stop* beam patterns are imaged onto each subsequent *pupil plane* passing outwards through the instrument and finally onto the telescope pupil at M2. Likewise the *detector* (horn aperture) patterns are imaged onto each intermediate *image plane* (field stop), but also spatially filtered by the intervening cold stop. E.g. as per fig.9.

This field-stop pattern is also imaged at the telescope image surface (just after the SPIRE instrument entrance), and finally also onto the sky. As the sky is at infinity, the beam pattern there is expressed as intensity versus far-field angle rather than radial position in mm, but the shape is unchanged, as is meant by the term 'imaging' in this context. Here the scaling from field stop position r to sky off-axis angle θ is

$$\theta = r.F_{\text{TEL}}/(F_{\text{FS}}f)$$

where F_{TEL} & F_{FS} are the telescope & field stop f-numbers, and f is the telescope focal length (28.5m, ref.7).

Therefore in this model there is no additional beam-clipping for components ahead of the cold-stop.

3.6 Features not included.

The above analysis assumes a 'perfect' instrument + telescope system in that all apertures ahead of the cold stop are well oversized with respect to the beam produced by the detector horn in combination with that stop. The used beam then 'sees' no surfaces other than the low emissivity mirrors, so there is little stray-light, and the instruments PSF response is simply calculable as the field stop beam pattern scaled onto the sky as above. The edge-clearance data of section 3.2 shows that this assumption is valid for most components.

The use of finite *field stops* (required to control radiant energy entering the low temperature instrument) means that the pupil imaging occurs with finite spatial resolution, so blurring the edges of the beam at subsequent pupil planes. The effect is not included above as no extra clipping is applied after that at the cold stop. This pupil-stop edge blurring is serious, as it can lead to increased stray-light if the pupil has a warm surround. The particular case of concern is that of the telescope pupil, as this is relatively hot, and that case is dealt with in detail in the next section.

The omission of the field stop clipping is acceptable for the spatial resolution analysis, because it will only affect the PSF at angles outside the range of the field stop, i.e. at approx. > 4 arcmins or > 1.3 arcmins in photometer or FTS. Thus it does not affect the PSF main lobe nor then the results of fig.8.

A diffraction-limited blurring of field-stop beam patterns occurs due the finite size of the intervening pupil, in an analogous way to pupil blurring. It too is not included in the current model, but it is of less concern than the pupil effect because (a) stray-light from field stop edges affects only detectors at the outer edges of the array, not all detectors (b) there are no 'hot' field stops; all such stops are within the instrument.

The leakage of stray-light via successive field- & pupil- stops is generally a concern in instruments where the thermal emission from these stops is significant. It arises not just from diffraction but also from aberrations & build tolerances, and in the SPIRE design there is allowance made for these (ref.2). It leads to the question of relative sizing of the stops, and to the Lyot stop arrangement. With multiple imaging stages the result is a 'cascading' of stop sizes to filter out diffractive stray light, but the price that is paid for this is useful beam size, i.e. throughput.

In SPIRE with emphasis on detection sensitivity the sizing issue has been considered in detail for the throughput/stray-light trade-off (ref.8), i.e. how large we can make the SPIRE pupil in order to fill the telescope aperture, without incurring too much stray-light. This work is summarised in the next section.

4. Beam patterns & stray-light in telescope.

The long-wave beam pattern in the telescope has been analysed as part of a previous photometer design (ref.9, file bolpht80). Here we reproduce in summary the telescope part. Although the telescope design

has changed since that analysis, the effect on beam patterns is a simple scaling, i.e. the patterns relative to the GO beam size (far-field) or F-number (near-field) are not significantly changed.

The telescope model is shown in figure 10.

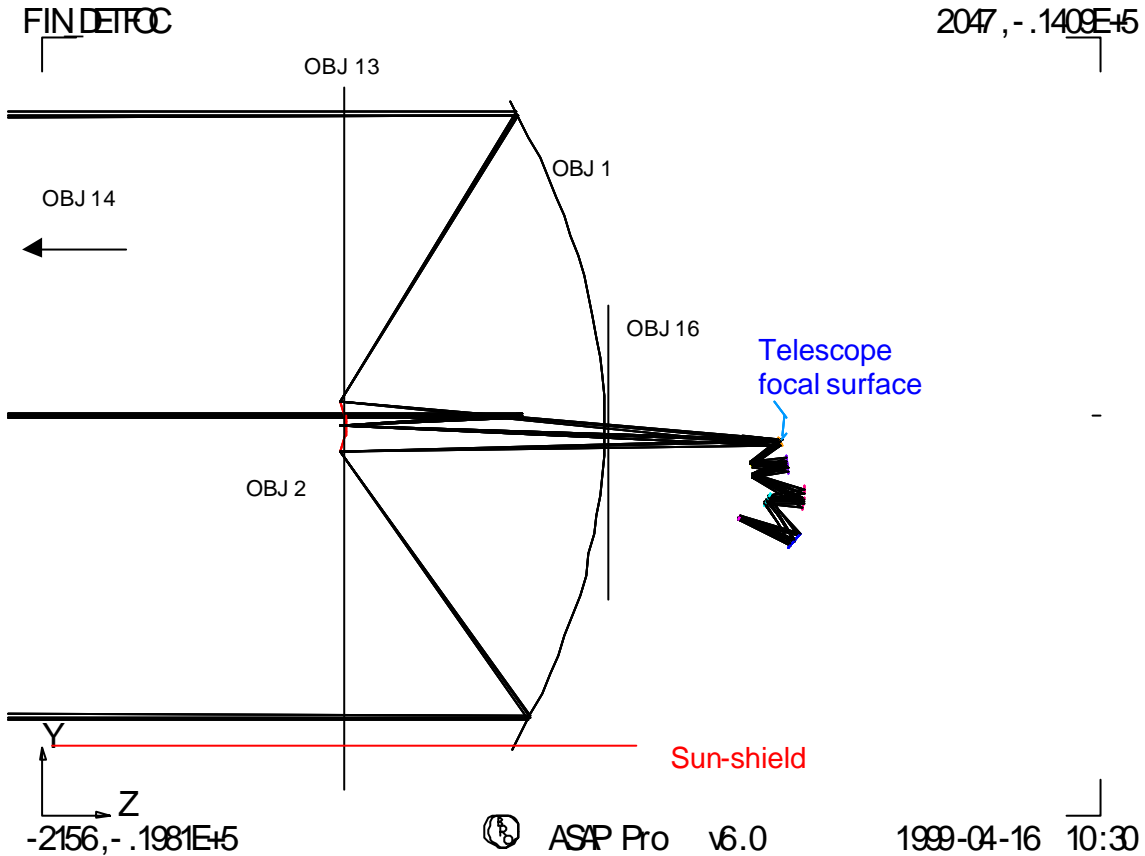
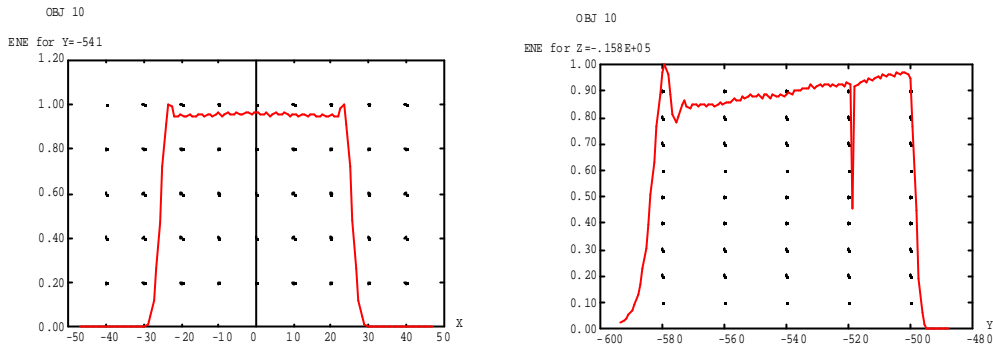


Figure 10. FIRST telescope model (bolpht80) & important surfaces.

The analysis is for the case of ‘bare’ detectors, considered as point-like (size $\ll 2F\lambda$), such that the beam pattern at the cold stop is that of a uniform intensity spherical wave (fig.11). This corresponds to a maximum pupil edge taper of 100 %, and is a worst case for stray-light. With the detectors now chosen as horn detectors with edge-taper $1/e^2$, the pupil-plane stray light estimates in refs 7 & 8 can be reduced by this factor.

4.1. Beam patterns.

Figures 11 - 15 show the intensity patterns at components passing outwards from the SPIRE field stop, for the on-axis beam, at $\lambda=0.5\text{mm}$.



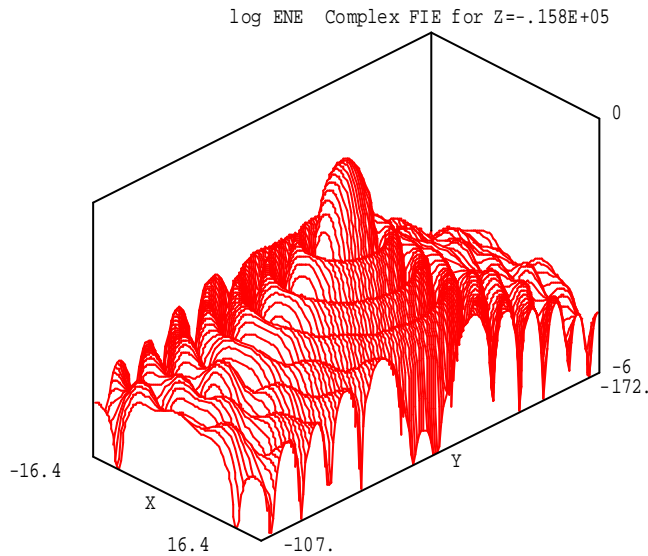
ASAP Pro v6.0

1999-04-19 14:33 ASAP Pro v6.0

1999-04-20 09:59

Fig.11. Beam pattern at Cold stop obj10, in X & Y sections.

BPH80B.apf RTRACE7.inr

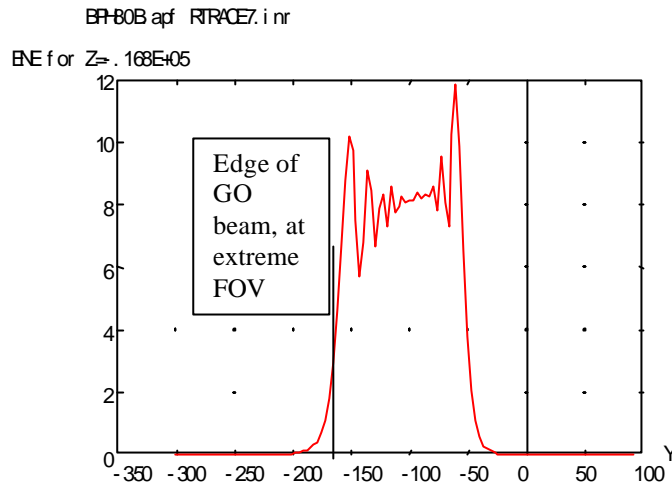


ASAP Pro v6.0

1999-04-21 08:44

Figure 12. Beam pattern as clipped at telescope focal surface, field stop 4' x 8'. Plot is intensity versus position in mm. Vertical scale is \log_{10} scale (10^{-6} to 10^0) to show extent of stop.

The beam pattern at the telescope cutout is shown in profile in figure 13.



ASAP Pro v6.0

1999-04-19 16:24

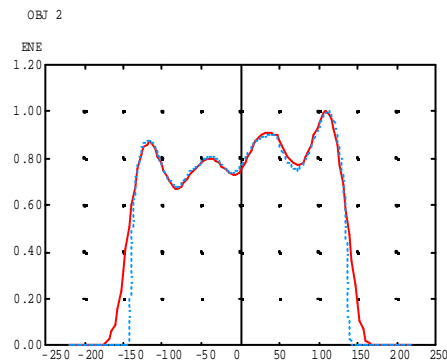
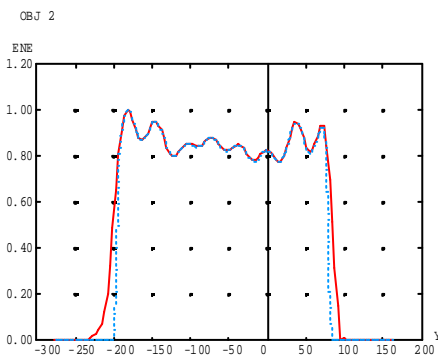
Figure 13. M1 cut-out. (Obj.16 in fig.10).

Here the ‘wings’ extend significantly outside the edge of the GO beam. For detectors near the array centre the cut-out edge is well away from the beam, and clipping & stray-light are low, but for those nearest the outer edge of the FIRST FOV, the GO beam appears to almost touch the cutout edge in the ray-trace (ref.1). In that case the clipping would be on one side of the beam, close to the geometric shadow as marked in the figure, producing significant stray-light (next section).

The beam pattern at M2, the telescope pupil, is shown in fig.14. This is a coherent image of that at the cold stop (instrument pupil), and so it should resemble the top-hat shape of fig.11. However it can be seen that it actually has a rippled profile & a significant slope on its sides, and both of these features are diffraction effects associated with the clipping (& spatial filtering) of the beam pattern by the field stop. The edge slope is attributable to diffraction-limited resolution in the filtered image of the cold-stop edge, with a blur diameter for this imagery of

$$b \approx 2.F_s.\lambda$$

where F_s is the f-number for the angle which the field stop subtends at M2. In the example $F_s \approx 50$ giving $b \approx 50\text{mm}$, i.e. the edge’s blur diameter is approx. 1/3 of the M2 aperture radius.



ASAP Pro v6.0

1999-04-21 08:36

1999-04-21 16:46

Figure 14. M2 mirror, Obj 2, in 2 sections.
Solid line = incident beam, dotted line = clipped reflected beam.

The figure 14 also shows how this beam pattern will be clipped by the edge of M2. Here there is no diffraction undersizing of the cold stop relative to M2, & so the clipping is significant. (If a horn detector beam were modeled, the clipping level would be reduced according to the pupil edge taper of that beam). The consequences of this clipping of the beam by M2 are (1) The detector beam 'sees' the surround of M2. (2) Out-of-field radiance incident on the M2 edge can, by being diffracted there, enter the detector beam. An example of this is radiance emitted by the sun-shield, considered in the next section.

In order to avoid the associated stray-light, the undersizing of the instrument cold stop could include an edge-diffraction allowance, to make it an effective Lyot stop at long wavelength (i.e. the SPIRE detector beam (or pupil) is made smaller than the telescope pupil to reduce its clipping by M2). However at this wavelength the diffractive undersize required is approx. half the blur diameter, i.e. 15 %, which would be unacceptable to the throughput requirement (affecting it across all wavelengths). An alternative might be to open up the field stop to reduce the blur diameter, but this is not possible due to the constraints from the other instruments & other stray-light requirements. It is therefore necessary to consider in greater detail whether the stray-light effects for a design without diffractive undersizing could be acceptable. Note that, because there are undersizes allowed for pupil aberration (pupil 'wander' with FOV position) & build tolerances, the beam clipping will actually not be symmetrical on each side (as per fig.14). Rather the clipping level shown is the worst case level which could be reached only on one side of the beam for any particular pupil alignment (all pixels) or FOV position (per pixel).

For the view of the M2 surround, there is no problem because the spillover part of the beam simply views cold space at this wavelength (in an annulus or cone centred on the FOV, & of half-angle 3.2 degrees). Part of the surround is occupied by the spider legs, but these are reflective & have bevelled edges to also view to space rather than to the sun-shield (ref.7).

Figure 15 shows the pattern at M1, due to the beam clipped by M2 as per the previous figure. In this case the beam pattern has sharply defined edges. This is because the beam size is \gg wavelength at M2, so additional spreading relative to the GO beam from M2 to M1 is minimal. This confirms that it is better to clip the beam (i.e. locate the pupil) at M2 than at M1 because M1 has the much hotter surround.

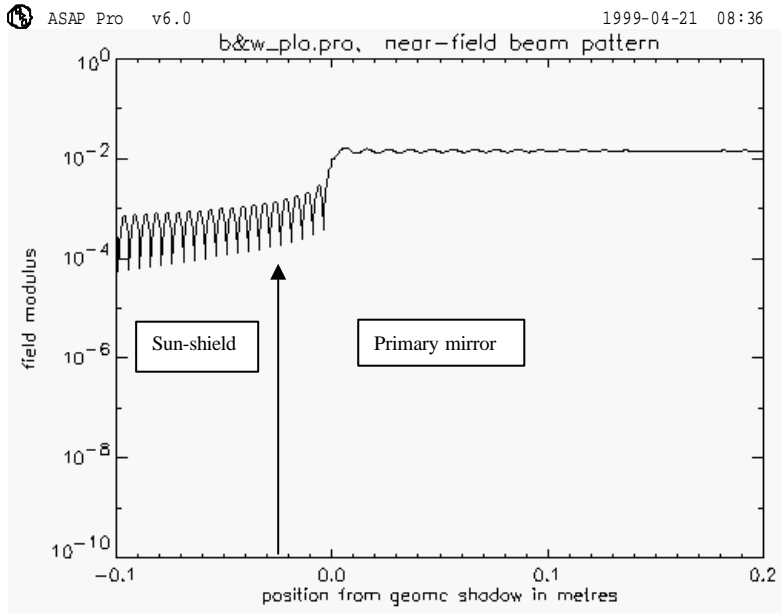
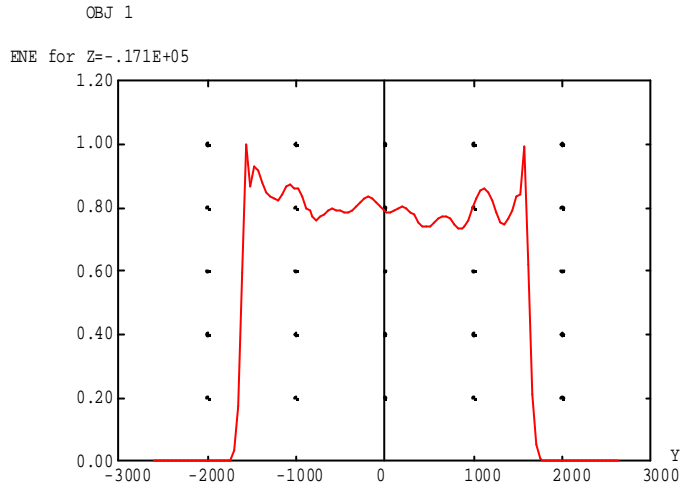


Figure 15. Beam pattern at M1. (a) Main beam (b) Sun-shield edge of beam in greater detail (log scale).

Although the beam pattern here has sharp edges, the sunshield lies quite close to the beam, so it is necessary to calculate the beam pattern down to lower levels than are shown in figure 15a. The propagation model does not have sufficient accuracy for this, and so instead the analytic diffraction equation for a top-hat (spherical wave) beam is used. This analysis is given in ref.11, and here in fig.15b the pattern near the beam edge is reproduced.

The worst-case position of the M1/sunshield boundary is shown in the figure, & is calculated as:

$$Y = o + (a-r).L$$

Where o = M1 oversize in mm = 17mm.

r = SPIRE FOV worst case = 13.5 arcmin for outer corner.

a = FIRST unvignetted FOV radius = 15 arcmin.

L = FIRST entrance pupil distance from M1 = 17 m.
 (ref.7), giving
 Y=24mm

4.2. Stray-light levels.

Here we estimate the diffractive stray-light terms from the above beam patterns. These terms are a sub-set of the overall stray-light analysis which for the telescope is given in ref.12.

For the components where part of the pattern lies on the surround, the detector partly sees the surround which can incorporate surfaces within the spacecraft having larger emissivity than the mirrors (viewed either directly or via further reflections) . The surround thereby contributes on-board thermal emission to the background level.

This diffractive stray-light varies with detector position in the array, increasing as we go from the centre of the array outwards, introducing more severe clipping at component edges. The exception to this is components near pupil planes, such as M2, where the beams from each detector are co-incident, so that the clipping is similar at all positions in the field. The clipping also varies with wavelength, becoming more severe at longer wavelengths, and the case considered is $\lambda=0.5\text{mm}$, i.e. beam-shape as per the above plots.

The clipping-background levels are expressed as a fraction η of the level due to the primary & secondary mirrors, as this is near to the level of the ideal BLIP condition. This fraction is written

$$SL = \frac{\epsilon_s \cdot P(T_s) \cdot B_s}{2 \cdot \epsilon_m \cdot P(T_m)}$$

where ϵ : emissivity
 P(T) black body Planck function.
 T temperature.
 B_s is the fraction of the beam flux which is on the surround surface.

And the subscripts s and m denote surround and telescope mirror emissivities respectively. The factor 2 in the denominator is to account for the two telescope mirrors.

The actual wavelength-dependence of B_s should require that the analysis is repeated over the range of wavelengths, whereas here we use only $\lambda=0.5\text{mm}$ as an average.

The beam fractions calculated from the above beam patterns, and resulting stray-light estimates are tabulated below.

Telescope component	Beam fraction on surround B _s	Surround emissivity	Source temp.	Background level SL	Reference

M1 cut-out, edge of FOV	0.02	0.15 (cryostat)	80 K	0.15	Fig.13
M2 surround Non-spider, (space viewing)	0.13	1	Cold space	0	Fig.14
M2 surround Spider	0.13x 1/16	0.02	Telescope 76 K	0.01	“
M1 surround Sun-shield, edge of FOV	2E-4	0.04	160 K	2e-3	Ref.9

Table 3. Stray light level from M2 surround (a) top-hat & (b) gaussian cases.

The M1 surround term is equivalent to edge-diffraction at M2, and this will be affected (further attenuated) by the modification (beveling or roughening) of the M2 edge as proposed for elimination of standing wave problems in HI-FI.

The largest stray-light term here is that for the M1 cutout, highlighted as a potential problem also in ref.11. However the above estimate can be scaled by $1/e^2$ since horn detectors are to be used, & so becomes **0.02**. Also it only applies to the edge of the FOV.

In conclusion, none of the SL levels due to diffractive beam propagation in the telescope are problematic at 0.5mm wavelength.

5. Referenced documents.

1. “Beam pattern (diffraction) effects in design of SPIRE instrument” SPIE Vol.4013. [SPIRE-RAL-PUB-000372](#).
2. “Optical system design description” [SPIRE-LAM-DOC-](#)
3. “Long-wavelength imaging effects in FTS” SPIRE-RAL-N000 430.
4. “Beam-mode model of FTS” SPIRE-RAL-N000 269.
5. “Beam patterns in FTS for the case of smooth-walled horn detectors” SPIRE-RAL-NOT-000 316.
6. “Beam patterns in photometer for the case of smooth-walled horns” SPIRE-RAL-NOT-000 431.
7. “Optical design of the ultra-light-weight FIRST telescope” SPIE Vol.4013. [SPIRE-REF-PUB-000409](#) & [SPIRE-REF-PUB-000411](#)
8. “Trade-off in beam shape & size in telescope” SPIRE-RAL-NOT-000118.
9. “Beam patterns ... in instrument & telescope” SPIRE-RAL-NOT-000101.01 Chapter 9.
10. MM-wave optics lecture notes, section 16.3. D.H.Martin, QMW College.
11. “Comparing sun-shield & primary mirror diffraction”. SPIRE-RAL-NOT-000 432.
12. “FIRST stray-light analysis & control” Eri Cohen, JPL.